

## POYNTING JETS FROM ACCRETION DISKS

R. V. E. LOVELACE,<sup>1</sup> H. LI,<sup>2</sup> A. V. KOLDOBA,<sup>3</sup> G. V. USTYUGOVA,<sup>4</sup> AND M. M. ROMANOVA<sup>1</sup>

Received 2001 June 11; accepted 2002 February 15

### ABSTRACT

We give further consideration to the problem of the evolution of a coronal, force-free magnetic field that threads a differentially rotating, conducting Keplerian disk, extending the recent work of Li and coworkers. This situation is described by the force-free Grad-Shafranov (GS) equation for the flux function  $\Psi(r, z)$  that labels the poloidal field lines (in cylindrical coordinates). The GS equation involves a function  $H(\Psi)$  describing the distribution of the poloidal current, which is determined by the differential rotation or “twist” of the disk that increases linearly with time. We numerically solve the GS equation in a sequence of volumes of increasing size corresponding to the expansion of the outer perfectly conducting boundaries at  $(R_m, Z_m)$ . The outer boundaries model the influence of an external nonmagnetized plasma. The sequence of GS solutions provides a model for the dynamical evolution of the magnetic field in response to (1) the increasing twist of the disk and (2) the pressure of external plasma. We find solutions with magnetically collimated Poynting jets in which there is a *continuous* outflow of energy, angular momentum, and toroidal magnetic flux from the disk into the external space. This behavior contradicts the commonly accepted “theorem” of solar plasma physics that the motion of the footpoints of a magnetic loop structure leads to a stationary magnetic field configuration with zero power, angular momentum, and flux outflows. In addition, we discuss magnetohydrodynamic simulations that show quasi-stationary collimated Poynting jets similar to our GS solutions. In contrast with the GS solutions, the simulations show a steady uncollimated hydromagnetic (nonforce-free) outflow from the outer part of the disk. The Poynting jets are of interest for the understanding of the jets from active galactic nuclei, microquasars, and possibly gamma-ray burst sources.

*Subject headings:* accretion, accretion disks — MHD

### 1. INTRODUCTION

Highly collimated, oppositely directed jets are observed in active galaxies and quasars (see, e.g., Bridle & Eilek 1984) and in old compact stars in binaries (Mirabel & Rodriguez 1994; Eikenberry et al. 1998). Further, well-collimated emission-line jets are seen in young stellar objects (Mundt 1985; Büehrke, Mundt, & Ray 1988). Recent work favors models in which the twisting of an ordered magnetic field threading an accretion disk acts to magnetically accelerate the jets (Meier, Koide, & Uchida 2001). There are two regimes: (1) the hydromagnetic regime, in which energy and angular momentum are carried by both the electromagnetic field and the kinetic flux of matter, which is relevant to the jets from young stellar objects; and (2) the Poynting flux regime, in which energy and angular momentum from the disk are carried predominantly by the electromagnetic field, which is relevant to extragalactic and microquasar jets and possibly to gamma-ray burst sources.

Stationary Poynting flux–dominated jets have been found in axisymmetric magnetohydrodynamic (MHD) simulations of the opening of magnetic loops threading a Keplerian disk (Romanova et al. 1998; Ustyugova et al. 2000). Theoretical studies have developed models for Poynting outflows from accretion disks (Lovelace, Wang, & Sulkanen

1987; Colgate & Li 1998). The present work represents a continuation of the study by Li et al. (2001), in which self-consistent, axisymmetric, nonrelativistic solutions of the Grad-Shafranov (GS) equation are calculated inside given conducting boundaries. The solutions are self-consistent in the respect that the twist of each field line is that due to the differential rotation of a Keplerian disk.

In § 2 we summarize the theory, and in § 3 we discuss the different types of solutions found. In § 4 we develop an analytic model for Poynting jets. In § 5 we discuss the consequences of expanding the boundaries. Sections 6–9 discuss the relevant conservation laws. In § 10 we compare the Poynting outflows with centrifugally launched winds. In § 11 we discuss the collapse of the inner part of the disk due to angular momentum outflow to Poynting jets. In § 12 we discuss conditions for occurrence of Poynting jets, including the influence of the kink instability. In § 13 we give results of MHD simulations that give Poynting jets similar to our GS solutions. Section 14 gives conclusions from this work.

### 2. THEORY OF POYNTING OUTFLOWS

Here, we consider further the theory of Poynting outflows (Li et al. 2001). We assume that magnetic field loops thread a differentially rotating, highly conducting Keplerian accretion disk at some initial time  $t = 0$ . Above the disk, we assume a “coronal” or force-free magnetic field in the nonrelativistic limit. This situation is described by the force-free GS equation for the flux function  $\Psi(r, z)$ , which labels the poloidal field lines (in cylindrical coordinates). The GS equation involves a function  $H(\Psi)$  that describes the distribution of poloidal current, which is determined by the differential rotation or

<sup>1</sup> Department of Astronomy, Cornell University, Ithaca, NY 14853-6801; rv11@cornell.edu, romanova@astrosun.tn.cornell.edu.

<sup>2</sup> Theoretical Astrophysics, T-6, MS B288, Los Alamos National Laboratory, Los Alamos, NM 87545; hli@lanl.gov.

<sup>3</sup> Institute of Mathematical Modeling, Russian Academy of Sciences, Moscow 125047, Russia; koldoba@spp.keldysh.ru.

<sup>4</sup> Keldysh Institute of Applied Mathematics, Russian Academy of Sciences, Moscow 125047, Russia; ustyugg@spp.keldysh.ru.

“twist” of the disk that increases linearly with time. We numerically solve the GS equation in a sequence of volumes of increasing size corresponding to the expansion of the outer perfectly conducting boundaries at  $(R_m, Z_m)$ . The outer boundaries model the influence of an external nonmagnetized plasma. The sequence of GS solutions provides a model for the dynamical evolution of the magnetic field in response to (1) the increasing twist of the disk and (2) the pressure of external plasma.

Cylindrical  $(r, \phi, z)$  coordinates are used, and axisymmetry is assumed. Thus, the magnetic field has the form  $\mathbf{B} = \mathbf{B}_p + B_\phi \hat{\phi}$ , with  $\mathbf{B}_p = B_r \hat{r} + B_z \hat{z}$ . We can write  $B_r = -(1/r)(\partial\Psi/\partial z)$ ,  $B_z = (1/r)(\partial\Psi/\partial r)$ , where  $\Psi(r, z) \equiv rA_\phi(r, z)$ . In the force-free limit, the magnetic energy density  $\mathbf{B}^2/(8\pi)$  is much larger than the kinetic or thermal energy densities; that is, the flow speeds are sub-Alfvénic,  $v^2 \ll v_A^2 = \mathbf{B}^2/4\pi\rho$ , where  $v_A$  is the Alfvén velocity. In this limit,  $0 \approx \mathbf{J} \times \mathbf{B}$ ; therefore,  $\mathbf{J} = \lambda\mathbf{B}$  (Gold & Hoyle 1960). Because  $\nabla \cdot \mathbf{J} = 0$ ,  $(\mathbf{B} \cdot \nabla)\lambda = 0$ , and consequently  $\lambda = \lambda(\Psi)$ , as is well known. Thus, Ampère’s equation becomes  $\nabla \times \mathbf{B} = 4\pi\lambda(\Psi)\mathbf{B}/c$ . The  $r$  and  $z$  components of Ampère’s equation imply

$$rB_\phi = H(\Psi), \quad \frac{dH(\Psi)}{d\Psi} = \frac{4\pi\lambda(\Psi)}{c},$$

where  $H(\Psi)$  is another function of  $\Psi$ . Thus,  $H(\Psi) = \text{const}$  are lines of constant poloidal current density;  $\mathbf{J}_p = (c/4\pi)(dH/d\Psi)\mathbf{B}_p$  so that  $(\mathbf{J}_p \cdot \nabla)H = 0$ . The toroidal component of Ampère’s equation gives

$$\Delta^* \Psi = -H(\Psi) \frac{dH(\Psi)}{d\Psi}, \quad (1)$$

with  $\Delta^* \equiv \partial^2/\partial r^2 - (1/r)(\partial/\partial r) + \partial^2/\partial z^2$ , which is the GS equation for  $\Psi$  (see, e.g., Lovelace et al. 1987; Li et al. 2001).

Ampère’s law gives  $\oint d\mathbf{l} \cdot \mathbf{B} = (4\pi/c) \int d\mathbf{S} \cdot \mathbf{J}$ , so that  $rB_\phi(r, z) = H(\Psi)$  is  $(2/c)$  times the current flowing through a circular area of radius  $r$  (with normal  $\hat{z}$ ) labeled by  $\Psi(r, z) = \text{const}$ . Equivalently,  $-H[\Psi(r, 0)]$  is  $(2/c) \times$  the current flowing into the area of the disk  $\leq r$ . For all cases studied here,  $-H(\Psi)$  has a maximum so that the total current flowing into the disk for  $r \leq r_m$  is  $I_{\text{tot}} = (2/c)(-H)_{\text{max}}$ , where  $r_m$  is such that  $-H[\Psi(r_m, 0)] = (-H)_{\text{max}}$  so that  $r_m$  is less than the radius of the O-point,  $r_0$ . The same total current  $I_{\text{tot}}$  flows out of the region of the disk  $r = r_m$  to  $r_0$ .

We consider an initial value problem in which the disk at  $t = 0$  is threaded by a dipole-like poloidal magnetic field. The form of  $H(\Psi)$  is then determined by the differential rotation of the disk; the azimuthal *twist* of a given field line going from an inner footpoint at  $r_1$  to an outer footpoint at  $r_2$  is fixed by the differential rotation of the disk. The field line slippage speed through the disk due to the disk’s finite magnetic diffusivity is estimated to be negligible compared with the Keplerian velocity. For a given field line, we have  $r d\phi/B_\phi = ds_p/B_p$ , where  $ds_p \equiv (dr^2 + dz^2)^{1/2}$  is the poloidal arc length along the field line, and  $B_p \equiv (B_r^2 + B_z^2)^{1/2}$ . The total twist of a field-line loop is

$$\Delta\phi(\Psi) = \int_1^2 ds_p \frac{-B_\phi}{rB_p} = -H(\Psi) \int_1^2 \frac{ds_p}{r^2 B_p}, \quad (2)$$

with the sign included to give  $\Delta\phi > 0$ . For a Keplerian disk around an object of mass  $M$ , the angular rotation is

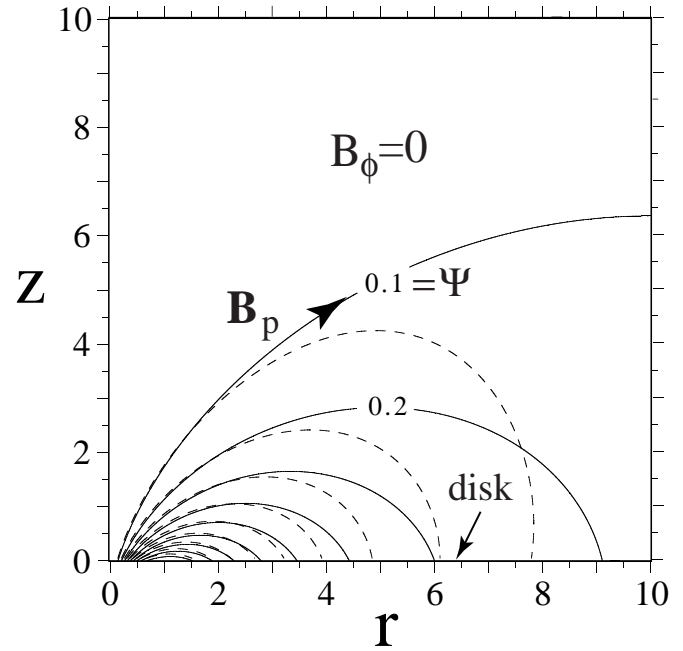


FIG. 1.—“Initial” dipole-like vacuum magnetic field. In this and subsequent plots,  $r$  and  $z$  are measured in units of the radius  $r_0$  of the O-point in the disk plane. The solid lines are the magnetic field lines for the case in which the flux function on the disk surface is  $\Psi(r, z=0) = a^3 r^2 K / (a^2 + r^2)^{3/2}$  with  $a = r_0 / \sqrt{2}$ . In this and subsequent plots,  $\Psi$  is measured in units of  $\Psi_0 = r_0^2 K / 3^{3/2}$ . Note that  $B_z(0) = 6\sqrt{3}\Psi_0/r_0^2 \approx 10.4\Psi_0/r_0^2$ . The dashed lines are the field lines for the case in which the outer boundaries ( $R_m = 10$ ,  $Z_m = 10$ ) are perfectly conducting; for this case,  $\Psi(r, z=0) \rightarrow \Psi(r, 0)[1 - (r/r_0 - 1)^2/81]$ , so that the O-point is still at  $r_0$ , and  $\Psi_0$  is unchanged. Because of axisymmetry and reflection symmetry about the  $z = 0$  plane, the field need only be shown in one quadrant.

$\omega_K = (GM/r^3)^{1/2}$ , so that the field-line twist after a time  $t$  is

$$\Delta\phi(\Psi) = \omega_0 t \left[ \left( \frac{r_0}{r_1} \right)^{3/2} - \left( \frac{r_0}{r_2} \right)^{3/2} \right] = (\omega_0 t) \mathcal{F} \frac{\Psi}{\Psi_0}, \quad (3)$$

where  $r_0$  is the radius of the O-point,  $\omega_0 \equiv (GM/r_0^3)^{1/2}$ , and  $\mathcal{F}$  is a dimensionless function (the quantity in the square brackets). The O-point is the point in the midplane of the disk encircled by the poloidal magnetic field lines; at this point  $\mathbf{B}_p = 0$ . At sufficiently small  $r_1$ , one reaches the inner radius of the disk  $r_i (\ll r_0)$ , where we assume  $\omega_K$  saturates at the value  $\omega_{Ki} = (GM/r_i^3)^{1/2}$ . For the dipole-like field of Figure 1,  $\mathcal{F} \approx 39^8 (\Psi_0/\Psi)^{3/4}$  for  $\Psi/\Psi_0 \ll 1$ , while  $\mathcal{F} \approx 3.64(1 - \Psi/\Psi_0)^{1/2}$  for  $1 - \Psi/\Psi_0 \ll 1$ .

For an accretion disk around a massive black hole  $M = M_8 10^8 M_\odot$  in the nucleus of galaxy, the twist is  $T = (t/3.17 \text{ days})(r_0/10^{15} \text{ cm})^{3/2}/\sqrt{M_8}$ . The inner radius of the disk is  $r_i \approx M_8(9 \times 10^{13}) \text{ cm}$  for a Schwarzschild black hole.

### 3. NUMERICAL SOLUTIONS OF GRAD-SHAFRANOV EQUATION

We solve equation (1) inside a cylindrical “box,”  $r = 0$  to  $R_m$  and  $z = 0$  to  $Z_m$ , with  $H(\Psi)$  determined by iteratively solving equations (1)–(3) (see Li et al. 2001; Finn & Chen 1990). The outer boundaries ( $r = R_m$  and  $z = Z_m$ ) are treated as conducting surfaces representing the interface

between the coronal  $\mathbf{B}$  field and external, nonmagnetized plasma. The external plasma will be pushed outward by the coronal field as it is twisted. Thus, we consider the  $\mathbf{B}$  field behavior as  $R_m \rightarrow \infty$  and  $Z_m \rightarrow \infty$ .

For a dipole-like field threading the disk (Fig. 1), it is natural to measure lengths in terms of the radius of the O-point in the disk,  $r_0$ . The natural value of the flux function  $\Psi$  is its maximum value at the O-point,  $\Psi_0$ . In turn, a natural unit for the magnetic field strength is  $\Psi_0/r_0^2$ . Notice that in the case of Figure 1,  $\Psi_0/r_0^2 \approx B_z(0)/10.4$ . Further, a natural unit for the total current (times  $c/2$ ),  $cI_{\text{tot}}/2 = (-H)_{\text{max}}$ , is  $\Psi_0/r_0$ . Also, we measure the total toroidal flux and the magnetic energy,

$$\Phi_t = \int dr dz B_\phi, \quad W_m = \frac{1}{4} \int r dr dz B^2, \quad (4)$$

in units of  $\Psi_0$  and  $\Psi_0^2/r_0$ , respectively. For boundary conditions, on the disk surface,  $\Psi(r, 0)$  is fixed and equal to its “initial” value on the disk because of the disk’s perfect conductivity. On the  $z$ -axis, we can take  $\Psi(0, z) = 0$ , because  $B_r = -(1/r)(\partial\Psi/\partial z) = 0$ . On the conducting outer boundaries,  $\Psi(r, Z_m) = 0$  and  $\Psi(R_m, z) = 0$ . Note, however, that in § 14 we discuss simulation results for the case of open outer boundaries. A uniform  $(r, z)$  grid of  $200 \times 200$  was used.

Figure 2 shows the behavior of a set of field solutions of equation (1) as the twist  $T = \omega_0 t$  is increased. The nature of the solutions changes dramatically as the twist increases above a critical value  $T_c \approx 1.14$  rad. For  $T < T_c$ , the nature of the field solutions is shown in Figures 3 and 4. The twisting of the field by the differential rotation of the disk “pumps” magnetic flux and energy into the disk corona, and the field tends to “inflate.” This behavior of coronal magnetic field loops of the Sun as a result of footpoint twisting is well known from the works of Aly (1984, 1991) and Sturrock (1991). The self-similar inflation of a force-free

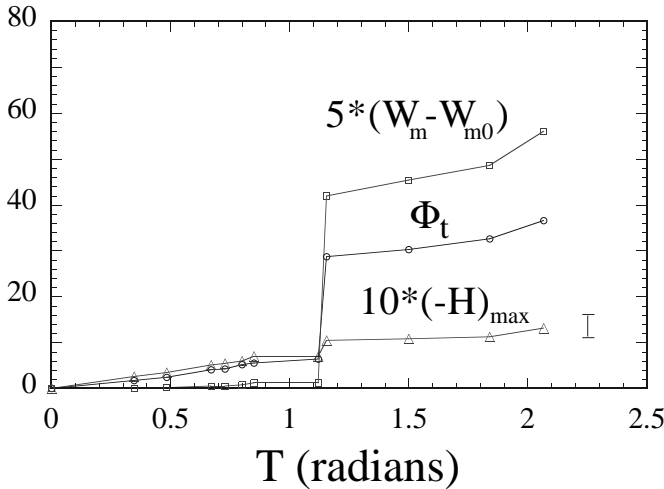


FIG. 2.—Summary of dependences of numerical solutions of eq. (1) on the twist  $T = \omega_0 t$ . For these solutions,  $H(\Psi)$  satisfies eqs. (2) and (3). Here,  $W_m$  is the magnetic energy (with  $W_{m0} \approx 0.57$  the energy for zero twist),  $\Phi_t$  is the toroidal flux, and  $(-H)_{\text{max}}$  is the total poloidal current (times  $c/2$ ). The solutions are inside a conducting box with  $R_m = 10 = Z_m$  for an initial dipole-like field with O-point at  $r_0 = 1$ , as shown by the dashed lines in Fig. 1. The value of  $T$  where the curves jump separates the two types of solutions found. The error bar indicates the estimated uncertainty in the values at  $T \sim 2$ , which results from the finite grid used in calculating  $\Delta\phi(\Psi)$ .

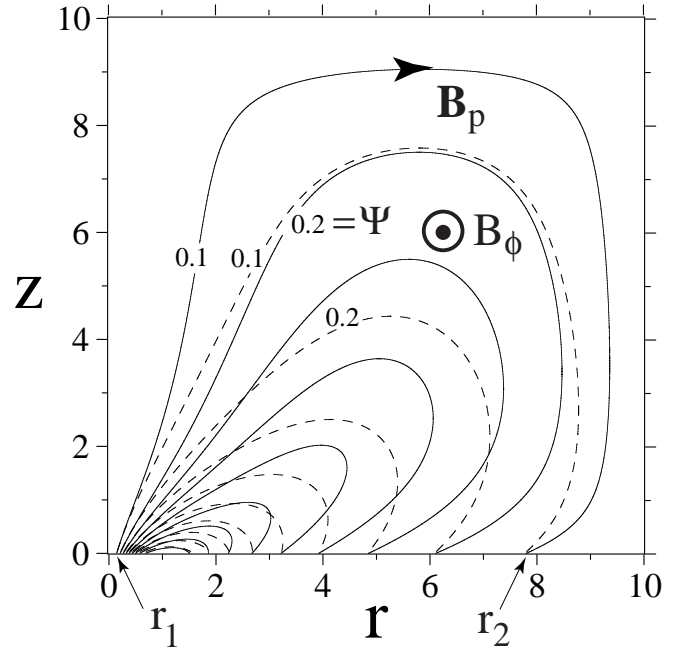


FIG. 3.—Poloidal field solutions for case of conducting boundaries for twists  $T = 0.67$  rad (dashed lines) and  $T = 1.1$  rad (solid lines). The initial poloidal magnetic field is shown by the dashed lines in Fig. 1.

field threading a non-Keplerian disk without outer boundaries was studied by Lynden-Bell & Boily (1994), and their solution for small twists is analogous to our low-twist solutions. The expansion of a force-free field into finite-pressure external plasma has been studied by Lynden-Bell (1996) and Li et al. (2001), and the poloidal field is found to fairly uniformly fill the coronal space.

For  $T > T_c$ , a new field configuration appears with a different topology. This is shown in Figure 5, where it is seen that a “plasmoid” consisting of toroidal flux has detached from the disk and is separated by the dashed field line, which has an X-point above the O-point on the disk. Figure 6 shows a three-dimensional view of two representative field lines for the same case. These high-twist equilibria consist of a region near the axis that is magnetically collimated by the toroidal  $B_\phi$  field, and a region far from the axis, on the outer radial boundary, which is anticollimated in the sense that it is pushed against the outer boundary. The field lines returning to the disk at  $r > r_0$  are anticollimated by the pressure of the toroidal magnetic field. The poloidal field fills only a small part of the coronal space. In a purely analytical analysis, Heyvaerts (2001) has independently found MHD equilibria involving the simultaneous formation of a collimated axial jet and an uncollimated outflow. Figure 6 shows a three-dimensional view of sample field lines.

As a test of our numerical solutions, note that conservation of axial momentum can be written as

$$\nabla \cdot (\mathbf{T} \cdot \hat{\mathbf{z}}) = 0, \quad \mathbf{T} \cdot \hat{\mathbf{z}} \equiv \frac{B^2 \hat{\mathbf{z}}}{8\pi} - \frac{B_z \mathbf{B}_p}{4\pi}. \quad (5)$$

Integration of equation (5) over the “box”  $(R_m, Z_m)$  gives

$$\int_0^{R_m} r dr (B_r^2 + B_\phi^2 - B_z^2)_{z=0} = \int_0^{R_m} r dr (B_r^2)_{z=Z_m}, \quad (6)$$

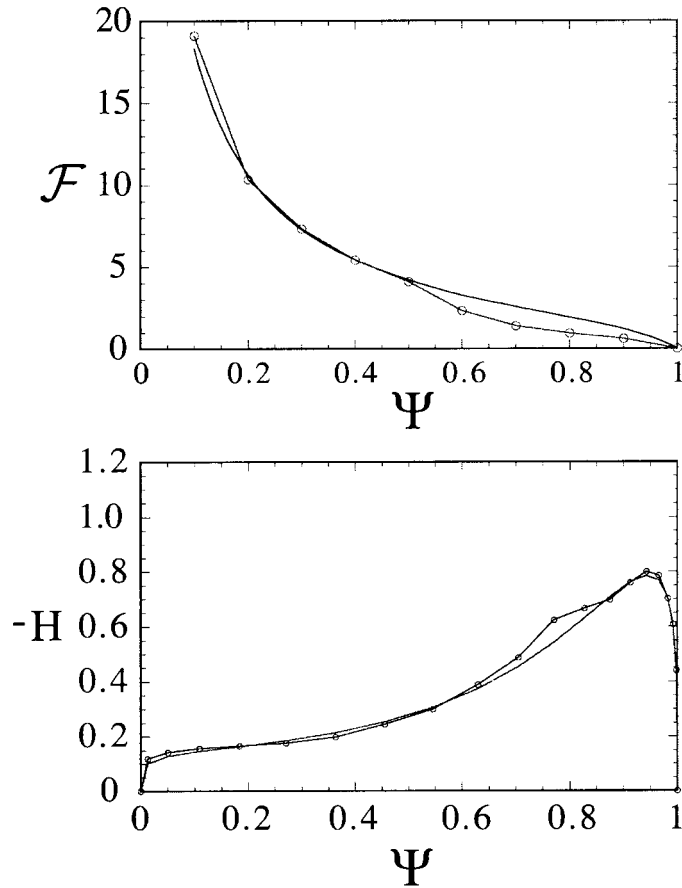


FIG. 4.—*Top*: The field-line twist function  $\mathcal{F}(\Psi)$ , with the circles indicating the derived numerical values and the smooth curve the theoretical dependence for a Keplerian disk given by eq. (3). The case shown corresponds to the solid field lines in Fig. 2, where the twist is  $T = 1.1$  rad. Here,  $\Psi$  is measured in units of  $\Psi_0$ , the value at the O-point. For this case, the bottom panel shows the poloidal current flow  $-H(\Psi)$  (in units of  $\Psi_0/r_0$ ), with the points indicating the numerical values and the smooth curve an analytic fit. The initial poloidal magnetic field is shown by the dashed lines in Fig. 1.

where the integral on the left-hand side represents the flux of momentum from the disk into the box, and the other integral the flux of momentum out of the top of the box. This equation is accurately satisfied by our numerical solutions; the typical errors are less than 0.1%.

#### 4. ANALYTIC SOLUTION FOR POYNTING JET

Most of the twist  $\Delta\phi$  of a field line of a Poynting jet occurs along the jet from  $z=0$  to  $Z_m$ . Because  $-r^2 d\phi/H(\Psi) = dz/B_z$ , we have

$$\frac{\Delta\phi(\Psi)}{-H(\Psi)} = \frac{(\omega_0 t)\mathcal{F}(\Psi/\Psi_0)}{-H(\Psi)} \approx \frac{Z_m}{r^2 B_z}, \quad (7)$$

where  $r^2 B_z(r, z)$  is evaluated on the straight part of the jet at  $r = r(\Psi)$ . In the core of the jet  $\Psi \ll \Psi_0$ , we have  $\mathcal{F} \approx 3^{9/8}(\Psi_0/\Psi)^{3/4}$ , and in this region we can take  $\Psi = C\Psi_0(r/r_0)^q$  and  $H = -\mathcal{K}(\Psi_0/r_0)(\Psi/\Psi_0)^s$ , where  $C$ ,  $q$ ,  $\mathcal{K}$ , and  $s$  are dimensionless constants. Equation (1) for the straight part of the jet implies  $q = 1/(1-s)$  and  $C^{2(1-s)} = s(1-s)^2 \mathcal{K}^2/(1-2s)$ . Thus, we find  $s = 1/4$ , so that  $q = 4/3$ ,  $C = (9/32)\mathcal{K}^{4/3}$ , and  $\mathcal{K} = 3^{1/8}4(r_0\omega_0 t/Z_m)$ .

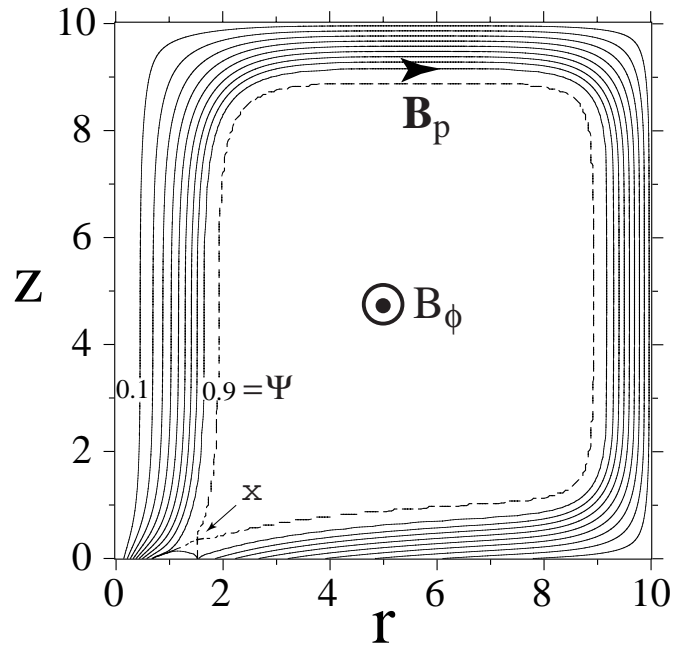


FIG. 5.—Poloidal field lines for Poynting jet case for twist  $T = 1.84$  rad and  $(-H)_{\max} = 1.13$ . The initial poloidal magnetic field is shown by the dashed lines in Fig. 1. The dashed contour is the separatrix with the X-point indicated. Note that the radial width of the upgoing field lines along the axis is about one-half the width of the downgoing field lines at the outer wall as required for equilibrium.

In order to have a Poynting jet, we find that  $\mathcal{K}$  must be larger than  $\approx 0.5$ . This corresponds directly to the condition  $T > T_c$  for the occurrence of the high-twist solutions. The condition arises from the fact that there is a competition between the buildup of toroidal flux inside the box due to twisting by the disk, which acts to increase  $B_\phi$ , and the expansion of the boundaries, which acts to decrease  $B_\phi$  (see § 12). If the boundaries expand too rapidly,  $B_\phi$  does not increase sufficiently to give a self-collimated Poynting jet. For the case of uniform expansion of the top boundary,  $Z_m = V_z t$ , this condition is the same as  $V_z < 9.2(r_0\omega_0)$ . For

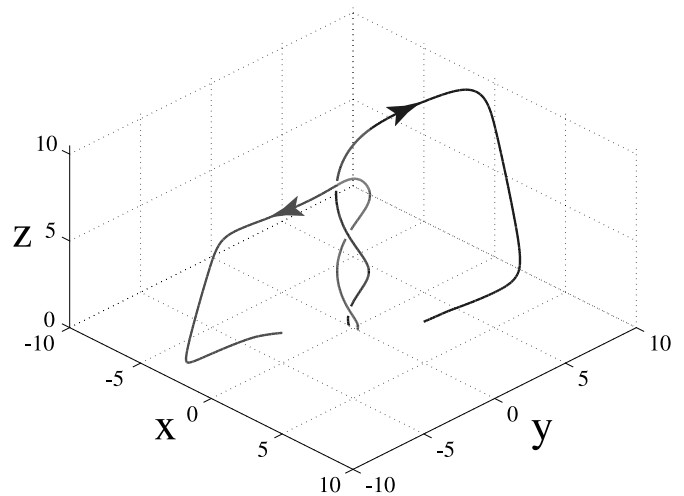


FIG. 6.—Three-dimensional view of two field lines originating from the disk at  $x = \pm 0.32r_0$  ( $\Psi = 0.4$ ) for the Poynting jet of Fig. 5. Each field line has a twist of  $\approx 8.22$  rad or about 1.31 rotations about the  $z$ -axis from its beginning at  $r_1$  and end at  $r_2$ . The  $z$ -axis is tilted toward the viewer by  $30^\circ$ .

the case of Figure 5,  $\mathcal{K} \approx 0.844$ . The field components in the straight part of the jet are

$$B_\phi = -\sqrt{2}B_z = -\sqrt{2}\left(\frac{3}{16}\right)^{1/3} \mathcal{K}^{4/3} \left(\frac{\Psi_0}{r_0^2}\right) \left(\frac{r_0}{r}\right)^{2/3}. \quad (8)$$

These dependences agree approximately with those found in numerical simulations of Poynting jets (Ustyugova et al. 2000). On the disk,  $\Psi \approx 3^{3/2}\Psi_0(r/r_0)^2$  for  $r < r_0/3^{3/4}$ . Using this and the formula for  $\Psi(r)$  gives the relation between the radius of a field line in the disk, denoted  $r_d$ , and its radius in the jet,  $r/r_0 = 6.5(r_d/r_0)^{3/2}\mathcal{K}^{-1}$ . Thus, the power law for  $\Psi$  is applicable for  $r_1 < r < r_2$ , where  $r_1 = 6.5r_0(r_i/r_0)^{3/2}/\mathcal{K}$  and  $r_2 = 1.9r_0/\mathcal{K}$ , with  $r_i$  the inner radius of the disk. The outer edge of the Poynting jet has a transition layer where the axial field changes from  $B_z(r_2)$  to zero, while (minus) the toroidal field increases from  $-B_\phi(r_2)$  to  $(-H)_{\max}/r_2$ . Using equation (6), which is only approximate at  $r_2$ , gives  $(-H)_{\max} \approx 1.2\mathcal{K}\Psi_0/r_0$ . This dependence agrees approximately with our GS solutions.

## 5. EXPANSION OF BOUNDARIES

The magnetic forces on the outer wall increase by a large factor in going from the low-twist to high-twist solutions. The radial force on the cylindrical wall and the axial force on the top wall are

$$F_r = \frac{1}{4}R_m \int_0^{Z_m} dz B_z^2 \Big|_{R_m}, \quad F_z = \frac{1}{4} \int_0^{R_m} r dr B_r^2 \Big|_{Z_m}. \quad (9)$$

For the low-twist solution of Figure 3 ( $T = 1.1$ ),  $(F_r, F_z) \approx (0.0061, 0.013)$ , whereas for the high-twist solution of Figure 5 ( $T = 1.79$ ),  $(F_r, F_z) \approx (0.26, 0.45)$  in units of  $(\Psi_0/r_0)^2$ .

Figure 7 shows the radial dependence of the magnetic pressure on the top boundary for the cases of low-twist and high-twist solutions.

Different behavior is exhibited by the low-twist and high-twist solutions as the conducting boundaries are moved outward. For the low-twist solutions, the poloidal field tends to expand outward to fairly uniformly fill the available space. As  $R_m \rightarrow \infty$  and  $Z_m \rightarrow \infty$ , we find that these solutions are

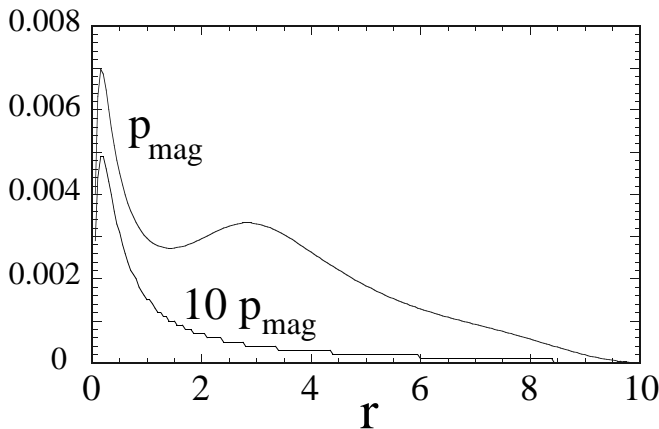


FIG. 7.—Radial dependences of the magnetic pressure  $p_{\text{mag}} = B^2(r, Z_m)/4\pi$  on the top boundary for the cases of high-twist ( $T = 1.79$ ; top curve) and low-twist ( $T = 1.1$ ; bottom curve) solutions. The pressure is in units of  $(\Psi_0/r_0^2)^2 \approx [B_z(0)/10.4]^2$ .

similar to those obtained by Lynden-Bell & Boily (1994), where there are no outer boundaries.

In contrast, for the high-twist solutions, the poloidal field near the axis maintains its collimation because of  $B_\phi$ , whereas the “return” poloidal field far from the axis is pushed against the outer cylindrical wall because of the  $B_\phi$  field. As  $R_m \rightarrow \infty$  and  $Z_m \rightarrow \infty$ , the collimated field near the axis will extend outward along the  $z$ -axis in the absence of instabilities. It is clear from Figure 7 that the magnetic pressure on the top boundary peaks near the axis. Thus, this region of the boundary should expand most rapidly in the physical case in which the boundary is an interface with external plasma.

Estimation of the axial expansion of a Poynting jet can readily be made, assuming that a region of radius  $\sim gr_2$  ( $g \sim 2-3$ ) of the jet expands with velocity  $V_z$  into a constant density external medium. For likely conditions,  $V_z$  is much larger than the sound speed in the external medium so that the ram pressure due to the jet motion is  $\rho_{\text{ext}}V_z^2$ , assuming  $(V_z/c)^2 \ll 1$  as required by our nonrelativistic treatment. Balancing this pressure with the magnetic pressure of the jet gives

$$\rho_{\text{ext}}V_z^2 \sim \frac{(-H)_{\max}^2}{4\pi g^2 r_2^2} \sim 0.14 \left[ \frac{B_z(0)}{g} \right]^2 \left( \frac{r_0\omega_0}{V_z} \right)^4,$$

or

$$V_z \sim (r_0\omega_0)^{2/3} \left[ \frac{B_z(0)}{g} \right]^{1/3} / \rho_{\text{ext}}^{1/6}. \quad (10)$$

The condition for a Poynting jet  $\mathcal{K} > 0.5$  corresponds to  $V_z < 9.2(r_0\omega_0)$ . For  $B_z(0) = 100$  G,  $r_0 = 10^{15}$  cm, and  $M = 10^8 M_\odot$ , the external density  $\rho_{\text{ext}}$  must be larger than  $\sim 2 \times 10^{-22}$  g cm $^{-3}$  in order to have  $V_z < c$ . For larger magnetic fields, a much larger external density is needed to give  $V_z < c$ . This points out the need for a relativistic treatment of the Poynting jet expansion.

## 6. ANGULAR MOMENTUM CONSERVATION

Conservation of angular momentum about the  $z$ -axis can be written as

$$\nabla \cdot \vec{\mathcal{J}} = 0, \quad \vec{\mathcal{J}} \equiv -\frac{r\mathbf{B}_p B_\phi}{4\pi} = -\frac{\mathbf{B}_p H}{4\pi}, \quad (11)$$

where  $\vec{\mathcal{J}}$  is the angular momentum flux-density vector. Integration of equation (11) over the “box”  $(R_m, Z_m)$  gives

$$0 = -\frac{1}{2} \int_0^{R_m} r dr H(B_z)_{z=0}. \quad (12)$$

The subscript  $z = 0$  here and subsequently indicates that the quantity is evaluated on the top surface of the disk. For a dipole-like field threading the disk where  $\Psi(R_m, 0) = 0 = \Psi(0, 0)$ , equation (12) gives

$$0 = -\frac{1}{2} \int_0^{\Psi_0} d\Psi H(\Psi) - \frac{1}{2} \int_{\Psi_0}^0 d\Psi H(\Psi). \quad (13)$$

The first integral represents the outflow of angular momentum from the inner part of the disk (interior to the O-point), and this equals the angular momentum inflow into the outer part of the disk given by the second integral.

The outflow of angular momentum from the inner part of the disk causes enhanced accretion of this part of the disk, whereas the inflow of angular momentum to the outer disk reduces the accretion rate. Because the Poynting outflows carry negligible matter, the continuity equation for the disk is

$$\frac{\partial \Sigma}{\partial t} + \nabla \cdot (\Sigma v_r \hat{\mathbf{r}}) = 0, \quad (14)$$

where  $\Sigma(r, t)$  is the surface mass density of the disk. The continuity equation for the disk angular momentum is

$$\frac{\partial(\Sigma l)}{\partial t} + \nabla \cdot (\Sigma v_r l \hat{\mathbf{r}} + \mathcal{F}_r^{\text{vis}} \hat{\mathbf{r}}) = \frac{r(B_\phi B_z)_{z=0}}{2\pi}, \quad (15)$$

where  $\mathcal{F}_r^{\text{vis}}$  represents the viscous transport of angular momentum in the disk, the term on the right-hand side is the outflow or inflow of angular momentum (from the two sides of the disk) due to the magnetic field, and  $l$  is the specific angular momentum of the disk matter. The disk is assumed almost Keplerian, so that  $l = (GMr)^{1/2} = rv_K$ , and consequently the two continuity equations give the mass accretion rate  $\dot{M} = \dot{M}_B + \dot{M}_{\text{vis}}$ ,

where

$$\dot{M}_B(r) \equiv -2\pi r \Sigma v_r = -2 \left( \frac{r^2}{v_K} \right) (B_\phi B_z)_{z=0} \quad (16)$$

is the ‘‘magnetically driven’’ mass accretion rate, and  $\dot{M}_{\text{vis}} = 6\pi\sqrt{r} d(\nu\sqrt{r}\Sigma)/dr$  is the viscous accretion rate with  $\nu$  the kinematic viscosity (Lovelace, Newman, & Romanova 1997). We have  $\dot{M}_B > 0$  (or less than 0) for  $r < r_0$  (or  $r > r_0$ ). The accretion speed is  $u \equiv -v_r = u_B + u_{\text{vis}}$ , with  $u_B = \dot{M}_B/(2\pi r \Sigma)$  and  $u_{\text{vis}} = \dot{M}_{\text{vis}}/(2\pi r \Sigma)$ .

Figure 8 shows the radial dependence of  $\dot{M}_B$  for a high-twist case. That  $\dot{M}_B$  due to the Poynting outflow is a function of  $r$  emphasizes the fact that disk is not stationary.

## 7. MAGNETIC FIELD TRANSPORT IN THE DISK

The poloidal magnetic field threading the disk tends to be advected inward with the accretion flow, but at the same time it may diffuse through the disk because of a finite magnetic diffusivity  $\eta_m$  of the disk. The continuity equation for poloidal flux through the disk  $B_z(r, 0, t)$  is

$$\frac{\partial B_z}{\partial t} + \nabla \cdot [v_r B_z \hat{\mathbf{r}} + \mathcal{U}_r B_z \hat{\mathbf{r}}] = 0, \quad (17)$$

where  $\mathcal{U}_r = (\eta_m/h) \tan(\theta)$  is the outward diffusive drift speed,  $h$  the half-thickness of the disk,  $\tan(\theta) \equiv (B_r/B_z)_{z=0}$ , and a smaller, second-order diffusion term ( $\eta_m \partial^2 B_z / \partial r^2$ ) has been omitted (see Lovelace et al. 1997). For cases in which the diffusivity is of the order of the viscosity and where the viscosity is given by the Shakura & Sunyaev (1973) prescription  $\nu = \alpha c_s h$  (with  $\alpha < 1$  and  $c_s$  the midplane sound speed), the diffusive drift speed is  $\mathcal{U}_r \sim \alpha c_s \tan(\theta)$ . For a strong magnetic field threading the disk, the accretion speed  $u$  in the inner part of the disk ( $r < r_0$ ) may be large with  $u_B \gg u_{\text{vis}}$  and  $u_B > \mathcal{U}_r$ , so that the disk flow advects the  $B_z(r, 0)$  field inward. On the other hand, at large radii, the magnitude of  $u$  is probably much smaller, so that the  $B_z(r, 0)$  field tends to drift outward,  $\mathcal{U}_r > u$ .

## 8. ENERGY CONSERVATION

We assume the coronal plasma is perfectly conducting, so that  $\mathbf{E} = -\mathbf{v} \times \mathbf{B}/c$ . For quasi-stationary and axisymmetric conditions,  $\nabla \times \mathbf{E} = 0$ , and thus  $E_\phi = 0$ , and  $\mathbf{E}_p = -\nabla\Phi$ , so that  $\mathbf{v}_p \propto \pm \mathbf{B}_p$ , and the electrostatic potential  $\Phi = \Phi(\Psi)$ . Thus,  $\mathbf{E} = -\Omega \nabla \Psi / c$ , with  $\Omega(\Psi) \equiv d\Phi(\Psi)/d\Psi$ . For the situations considered here, all field lines pass through the disk. At the disk surface,  $E_r(r, 0) = -(v_\phi)_{\text{disk}} B_z(r, 0)/c$ , since  $v_z = 0$ . Therefore,  $\Omega[\Psi(r, 0)] = (v_\phi)_{\text{disk}}/r$ .

For a force-free plasma, we have

$$\frac{\partial}{\partial t} \left( \frac{\mathbf{B}^2}{8\pi} \right) + \nabla \cdot \left( \frac{c}{4\pi} \mathbf{E} \times \mathbf{B} \right) = 0. \quad (18)$$

Integration of equation (18) over the ‘‘box’’ ( $r = 0$  to

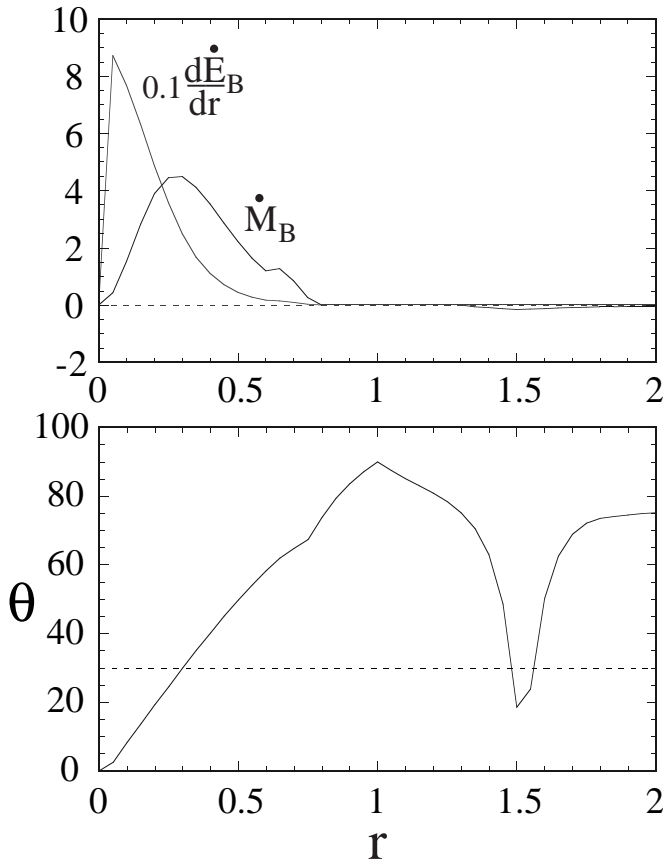


FIG. 8.—Top: Radial dependence of the mass accretion rate of the disk  $\dot{M}_B$  due to the Poynting outflow from the disk, and  $(0.1 \times)$  the Poynting power outflow per unit radius  $d\dot{E}_B/dr$  for quasi-stationary conditions. Bottom: The radial dependence of the angle between poloidal field lines and the  $z$ -axis at the disk surface,  $\theta = \tan^{-1}(|B_r/B_z|)$ . Both panels are for the high-twist case of Figs. 5–7. As mentioned, for  $\Psi > 0.95$  or  $0.764 < r < 1.33$ , the field lines are closed. In the interval  $1 < r < 1.5$ ,  $B_r/B_z$  is less than zero.

$R_m, z = 0$  to  $Z_m$ ) gives

$$\begin{aligned} \frac{dW_m}{dt} = & -\frac{1}{2} \int_0^{R_m} r dr (v_\phi B_\phi B_z)_{z=0} \\ & -\frac{1}{4} \dot{R}_{\max} R_m \int_0^{Z_m} dz B^2(R_m, z) \\ & -\frac{1}{4} \dot{Z}_m \int_0^{R_m} r dr B^2(r, Z_m), \end{aligned} \quad (19)$$

where  $W_m$  is the magnetic field energy in the box (eq. [4]). The second and third integrals in equation (19) represent the energy expended in “pushing” the boundaries outward (the  $p dV$  work). The first integral represents the outflow of energy from the inner part of the disk surface (inside the O-point) and the inflow into the outer part of the disk. For a dipole-like field threading the disk where  $\Psi(R_m, 0) = 0 = \Psi(0, 0)$ , the first integral for the power output from the disk can be rewritten as

$$-\frac{1}{2} \int_0^{\Psi_0} d\Psi \Delta\dot{\phi}(\Psi) H(\Psi) = \frac{\omega_0 \Psi_0^2}{2r_0} \int_0^1 d\tilde{\Psi} \tilde{\mathcal{F}}[-\tilde{H}(\tilde{\Psi})], \quad (20)$$

where  $\omega_0 \equiv (GM/r_0^3)^{1/2}$ , and the tildes indicate dimensionless variables. For the low-twist solution ( $T = 1.1$ ) of Figure 3, the dimensionless integral denoted  $\mathcal{I} \approx 1.75$ , whereas for the high-twist solution of Figure 5 ( $T = 1.84$ ),  $\mathcal{I} \approx 3.05$ . Thus,

$$\begin{aligned} \dot{E} \approx & 0.9 \times 10^{45} \text{ ergs s}^{-1} \left(\frac{\mathcal{I}}{3}\right) \left[\frac{B_z(0)}{3 \text{ kG}}\right]^2 \left(\frac{r_0}{10^{15} \text{ cm}}\right)^{3/2} \\ & \times \left(\frac{M}{10^8 M_\odot}\right)^{1/2} \end{aligned} \quad (21)$$

for the power output from the two sides of the disk.

The Poynting power outflow per unit radius from the two sides of the disk is

$$\frac{d\dot{E}_B}{dr} = -rv_K (B_\phi B_z)_{z=0} = \left(\frac{v_K^2}{2r}\right) \dot{M}_B \quad (22)$$

for quasi-stationary conditions. Figure 8 shows the radial dependence of  $d\dot{E}_B/dr$ , which indicates that most of the power outflow occurs in the inner part of the disk.

## 9. GENERATION OF TOROIDAL FLUX

Perfect conductivity and Faraday’s law imply

$$\frac{\partial \mathbf{B}}{\partial t} = \nabla \times (\mathbf{v} \times \mathbf{B}), \quad (23)$$

where  $\mathbf{v}$  is the plasma flow velocity. We apply this equation to a “box” extending from the disk at  $z = 0$  to a nonrotating, perfectly conducting surface at  $z = Z_m$ , and from the axis  $r = 0$  to a cylindrical, nonrotating, perfectly conducting surface at  $r = R_m$ . These outer surfaces are allowed to move, so that  $R_m$  and  $Z_m$  are generally time dependent. The toroidal flux  $\Phi_t$  (eq. [4]) obeys

$$\begin{aligned} \frac{d\Phi_t}{dt} = & \int_0^{R_m} dr (v_\phi B_z - v_z B_\phi) \Big|_0^{Z_m} \\ & - \int_0^{Z_m} dz (v_r B_\phi - v_\phi B_r) \Big|_0^{R_m}. \end{aligned} \quad (24)$$

On the top boundary,  $z = Z_m$ ,  $B_z = 0$ , and  $B_\phi = 0$ ; on the outer cylindrical boundary,  $r = R_m$ ,  $B_r = 0$ , and  $B_\phi = 0$ ; on the  $z$ -axis,  $B_\phi = 0$  and  $B_r = 0$ ; and on the disk,  $v_z(r, z = 0) = 0$ . Consequently, equation (24) simplifies to

$$\frac{d\Phi_t}{dt} = - \int_0^{R_m} dr v_\phi B_z(r, z = 0), \quad (25)$$

where  $v_\phi = (GM/r)^{1/2}$  is the azimuthal velocity of the disk. The integrand of equation (25) is independent of time in view of our assumption that  $\Psi(r, 0)$ , and thus,  $B_z(r, 0) = (1/r)\partial\Psi(r, 0)/\partial r$  is time independent.

For a dipole-like field threading the disk [where  $\Psi(r, 0)$  increases from zero to a maximum  $\Psi_0$  and then decreases to zero at  $r = R_m$ ], equation (25) can be rewritten as

$$\frac{d\Phi_t}{dt} = - \int_0^{\Psi_0} d\Psi \Delta\dot{\phi}(\Psi), \quad (26)$$

where  $\Delta\dot{\phi}(\Psi)$  is the time derivative of equation (3), which is independent of time. For the dipole-like field of Figure 1, evaluation of this integral gives  $d\Phi_t/dt \approx -12.1\omega_0\Psi_0 \approx -12.1\omega_0[B_z(0)/10.4]r_0^2$ . Thus,

$$\begin{aligned} \frac{d\Phi_t}{dt} \approx & -1.3 \times 10^{28} \frac{\text{G cm}^2}{\text{s}} \left[\frac{B_z(0)}{3 \text{ kG}}\right] \left(\frac{r_0}{10^{15} \text{ cm}}\right)^{1/2} \\ & \times \left(\frac{M}{10^8 M_\odot}\right)^{1/2} \end{aligned} \quad (27)$$

is the toroidal flux generation rate from one side of the disk.

## 10. POYNTING VERSUS CENTRIFUGAL OUTFLOWS

The centrifugal force near the surface of a Keplerian disk has a role in launching hydromagnetic outflows (Blandford & Payne 1982). The “centrifugal launching” requires that the field lines (projected into the poloidal plane) be tilted away from the  $z$ -axis by an angle  $\theta$  greater than  $30^\circ$ . The magnetic force, dominantly  $d(B_\phi^2/8\pi)/dz$ , is comparably important for launching hydromagnetic outflows (Love- lace, Berk, & Contopoulos 1991; Ustyugova et al. 1999); it also increases as  $\theta$  increases. Figure 8 shows the radial variation of  $\theta(r) = \tan^{-1}(|B_r/B_z|)_{z=0}$  for a high-twist case. For this case,  $\theta < 30^\circ$  for  $r < 0.3r_0$ , which includes the part of the disk giving the largest power output per unit radius,  $d\dot{E}_B/dr$ , shown in the top panel of Figure 8. Thus, there is a Poynting outflow under conditions where *no* centrifugal outflow occurs.

However, for the part of the disk at which  $\theta > 30^\circ$ , we predict a centrifugal hydromagnetic outflow with  $-(B_\phi B_z) > 0$  and inward magnetically driven accretion,  $u_B > 0$  (see Ustyugova et al. 1999). Hydromagnetic outflows from the region  $r > r_0$  are found in the MHD simulations discussed by Ustyugova et al. (2000) and in § 13.

## 11. COLLAPSE OF INNER DISK

Quasi-stationary Poynting jets from the two sides of the disk within  $r_0$  give an energy outflow per unit radius of the disk  $d\dot{E}_B/dr = rv_K(-B_\phi B_z)_h$ , where  $h$  indicates evaluation at the top surface of the disk. This outflow  $\sim r_0 d\dot{E}_B/dr \sim v_K(r_0)(\Psi_0/r_0)^2$  is estimated in equation (22), which agrees approximately with the values derived from the simulations (see § 14).

For long timescales, the Poynting jet is, of course, time dependent because of the angular momentum it extracts from the inner disk ( $r < r_0$ ). This loss of angular momentum leads to a “global magnetic instability” and collapse of the inner disk (Lovellace et al. 1997). An approximate model of this collapse can be made if the inner disk mass  $M_d$  is concentrated near the O-point radius  $r_0(t)$ , if the field-line slippage through the disk is negligible (see § 8),  $\Psi_0 = \text{const}$ , and if  $(-rB_\phi)_{\text{max}} \sim \Psi_0/r_0(t)$  (as found here). Then,  $M_d dr_0/dt = -2\Psi_0^2(GMr_0)^{-1/2}$ . If  $t_i$  denotes the time at which  $r_0(t_i) = r_i$  (the inner radius of the disk), then  $r_0(t) = r_i[1 - (t - t_i)/t_{\text{coll}}]^{2/3}$ , for  $t \leq t_i$ , where  $t_{\text{coll}} = (GM)^{1/2} M_d r_i^{3/2} / (3\Psi_0^2)$  is the timescale for the collapse of the inner disk. [Note that the timescale for  $r_0$  to decrease by a factor of 2 is  $\sim t_i(r_0/r_i)^{3/2} \gg t_i$  for  $r_0 \gg r_i$ .] The power output to the Poynting jets is

$$\dot{E}(t) = \frac{2\Delta E_{\text{tot}}}{3 t_{\text{coll}}} \left(1 - \frac{t - t_i}{t_{\text{coll}}}\right)^{-5/3}, \quad (28)$$

where  $\Delta E_{\text{tot}} = GMM_d/2r_i$  is the total energy of the outburst. Roughly,  $t_{\text{coll}} \sim 2 \text{ days } M_8^2 (M_d/M_\odot) \times (6 \times 10^{32} \text{ G cm}^2/\Psi_0)^2$  for a Schwarzschild black hole, where validity of the analysis requires  $t_{\text{coll}} \gg t_i$ . Such outbursts may explain the flares of active galactic nucleus blazar sources (Romanova & Lovellace 1997; Romanova 1999; Levinson 1998) and the one-time outbursts of gamma-ray burst sources (Katz 1997).

## 12. OCCURRENCE OF POYNTING JETS AND KINK INSTABILITY

The rate at which toroidal flux  $\Phi_t$  is created in the region above the disk is  $d\Phi_t/dt \approx -12\omega_0\Phi_0$  (see § 10). If the area  $R_m Z_m$  of this region is fixed because of a very dense external plasma, the average value of  $-B_\phi > 0$  in it increases. On the other hand, if the area  $R_m Z_m$  increases rapidly enough,  $-B_\phi$  will decrease. The Poynting jets occur under conditions in which  $-B_\phi$  increases to a sufficient extent to cause pinching of the poloidal magnetic field. Because the most rapid expansion of the  $\mathbf{B}$  field occurs in the  $z$ -direction, a necessary condition for occurrence of a Poynting jet is that the rate of expansion of the boundary  $V_z = dZ_m/dt$  be bounded by some constant. In fact, the condition obtained in § 4 for occurrence of Poynting jets has this form,  $V_z < 9.2(\omega_0 r_0)$ .

Note that there may be “self-regulation” in the respect that the field configuration that occurs is at the “boundary” between low- and high-twist solutions. In view of Figure 7, the low-twist field gives a gradual expansion of the boundaries, which allows buildup of toroidal flux, whereas the high-twist field gives a more rapid expansion, which tends to give a slower increase of  $\Phi_t$ .

The region of the collimated field (see Fig. 5)—the Poynting jet—has  $v^2 \ll v_A^2$  and is kink unstable according to the standard nonrelativistic analysis (e.g., Bateman 1980). The instability will lead to a helical distortion of the jet with the nonlinear amplitude of shift of the helix  $\Delta r \sim v_A t$ , and with the helix having the same twist about the  $z$ -axis as the axisymmetric  $\mathbf{B}$  field. Note, however, that for the astrophysical conditions of interest,  $v_A \equiv |\mathbf{B}|/(4\pi\rho)^{1/2}$  is likely to be larger than the speed of light. A relativistic perturbation analysis is then required, including the displacement current. The physical Alfvén speed is  $V_A = c/(1 + c^2/v_A^2)^{1/2} < c$ . Thus, the speed of lateral displacement of the helix is less than  $c$ .

The evolution of the Poynting jet evidently depends on *both*  $V_A$  and the velocity of propagation of the “head” of the jet  $V_z$  (§ 5), which may be relativistic. Relativistic propagation of the jet’s head may act to limit the amplitude of helical kink distortion of the jet. On the other hand, a subrelativistic propagation of the head may allow the helix amplitude to grow, but this amplitude can be limited by flux conservation as discussed by Kadomtsev (1963).

## 13. MHD SIMULATIONS OF POYNTING JETS

For the MHD simulations described here, the initial magnetic field has a dipole-like form, as shown in Figure 1. The computational region  $r = 0$  to  $R_{\text{max}}$ ,  $z = 0$  to  $Z_{\text{max}}$  is taken to have  $R_{\text{max}} = Z_{\text{max}} \approx 10r_0$ . Initially, the corona of the disk is in isothermal equilibrium without rotation. At  $t = 0$ , the disk starts to rotate with Keplerian velocity  $v_\phi(r, 0) = r\Omega_K$ , where  $\Omega_K = (GM)^{1/2}/(r^2 + r_i^2)^{3/4}$ , where the smoothing length  $r_i = 0.2r_0$  is interpreted as the inner radius of the disk. The smoothed gravitational potential is  $-GM/(r_i^2 + r^2)^{1/2}$ .

On the disk surface, the boundary conditions are as follows (Ustyugova et al. 2000). Two of the boundary conditions come from the fact that the tangential electric field  $(\mathbf{E}')_t$  in the frame rotating with the disk (at the Keplerian velocity) is zero;  $B_z$  at the disk surface is time independent, whereas  $B_r$  and  $B_\phi$  at the surface vary with time. Two further boundary conditions fix the entropy of the plasma coming out of the disk to be  $s_d(r)$  and the density of the outflowing plasma to be  $\rho_d(r)$ . If  $v_z$  at the disk surface, calculated by solving the MHD equations in the computational region, increases to the point where it is larger than the slow magnetosonic speed in the  $z$ -direction at the disk’s surface  $c_{\text{smz}}$ , then we clamp it to be equal to  $c_{\text{smz}}$ . This condition represents a limit on the mass efflux  $\rho v_z$  from the disk. For sub-slow magnetosonic outflow from the disk  $v_z < c_{\text{smz}}$ , we have four boundary conditions, whereas when  $v_z = c_{\text{smz}}$ , we have five boundary conditions.

For the outer boundaries, we first consider the case in which these surfaces are perfect conductors. Second, we consider the case of “free” outer boundaries, where  $\partial F_j/\partial n = 0$  on all scalar variables *except* for the toroidal magnetic field. For this field component, we take  $[\mathbf{B}_p \cdot \nabla(rB_\phi)] = 0$  on the outer boundaries, which was shown by Ustyugova et al. (1999) to avoid artificial collimation that can come from using the “free” boundary condition on  $rB_\phi$ . The free outer boundary conditions allow matter and Poynting flux to freely flow out through these surfaces.

For the cases we discuss, the strength of the poloidal magnetic field at the inner radius of the disk corresponds to  $(v_{Ap}/v_K)_i = 16.5$  and  $(c_s/v_K)_i = 1$ , where  $v_{Ap} \equiv |\mathbf{B}_p|/(4\pi\rho)^{1/2}$ . The  $i$  indicates evaluation at the inner radius of the disk  $r = r_i$  on the disk surface. In the midplane of the disk,  $(v_{Ap}/v_K)_{z=0}$  is less than or much less than unity. Different radial profiles of  $c_s$  on the disk surface have been used with similar results, including  $c_s/v_K = \text{const}$  and  $c_s = \text{const}$ ; the density profiles on the disk surface have been obtained as in Ustyugova et al. (1999).

Figure 9 shows the evolution of the coronal plasma for the case of fixed, conducting outer boundaries at  $(R_m, Z_m)$ . After about six rotation periods of the inner disk, the outgoing poloidal field collimates along the  $z$ -axis, and the returning poloidal field is pressed outward to the conducting walls. Most of the configuration is strongly field domi-

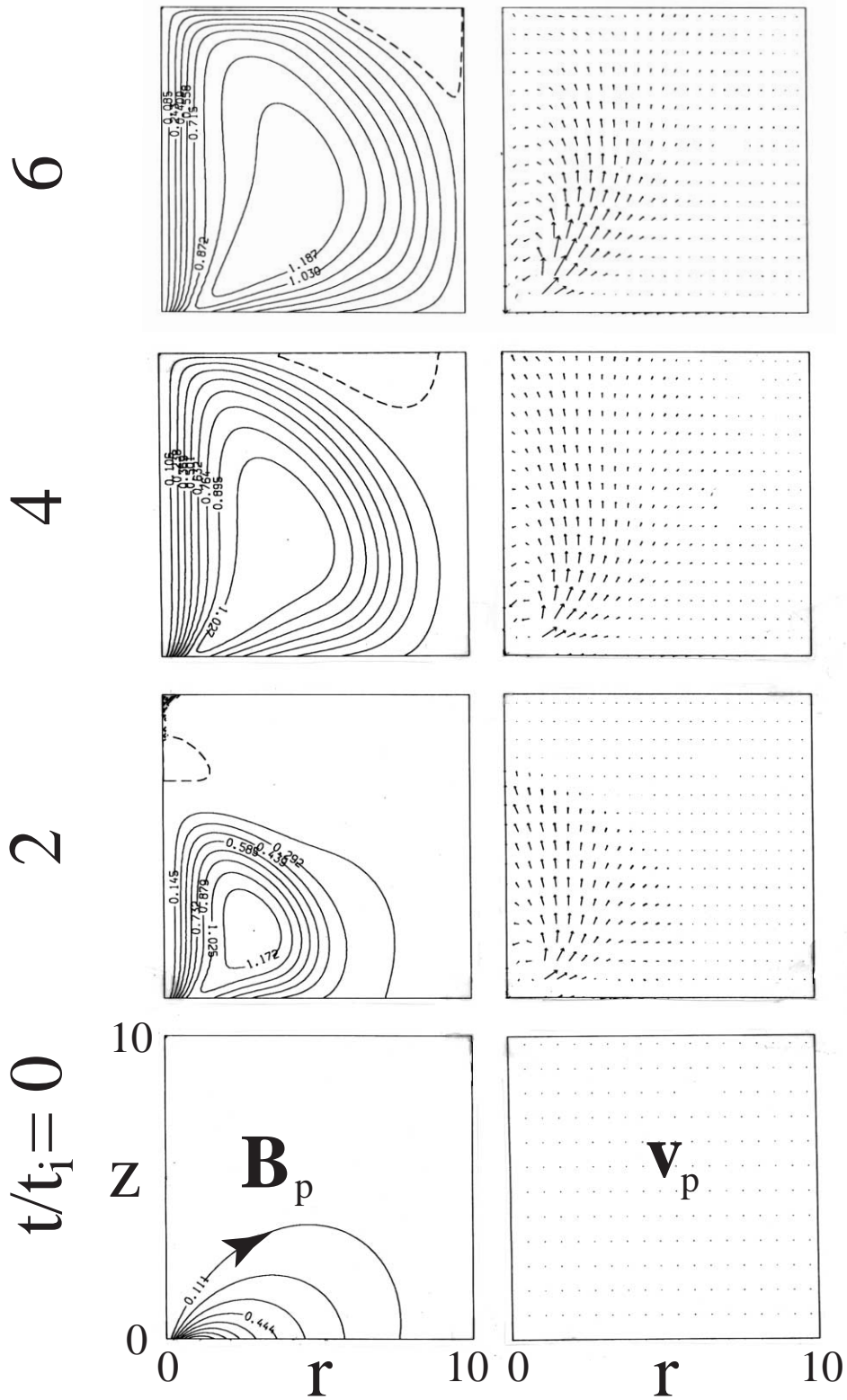


FIG. 9.—Time evolution of dipole-like field threading the disk from the initial configuration  $t = 0$  (bottom panels) for the case of conducting outer boundaries at  $R_m = 10$  and  $Z_m = 10$ . Here,  $t_i$  is the period of rotation at the inner radius of the disk  $r_i$ . The initial field is shown by the dashed lines in Fig. 1. The left-hand panels show the poloidal field lines, which are the same as  $\Psi(r, z) = \text{const}$  lines. The right-hand panels show the poloidal velocity vectors  $v_p$ . For this calculation, a uniform  $100 \times 100$  grid was used. For times longer than  $\sim 8t_i$ , the numerical calculations crash, apparently because of the buildup of fine-scale structure in the simulation region.

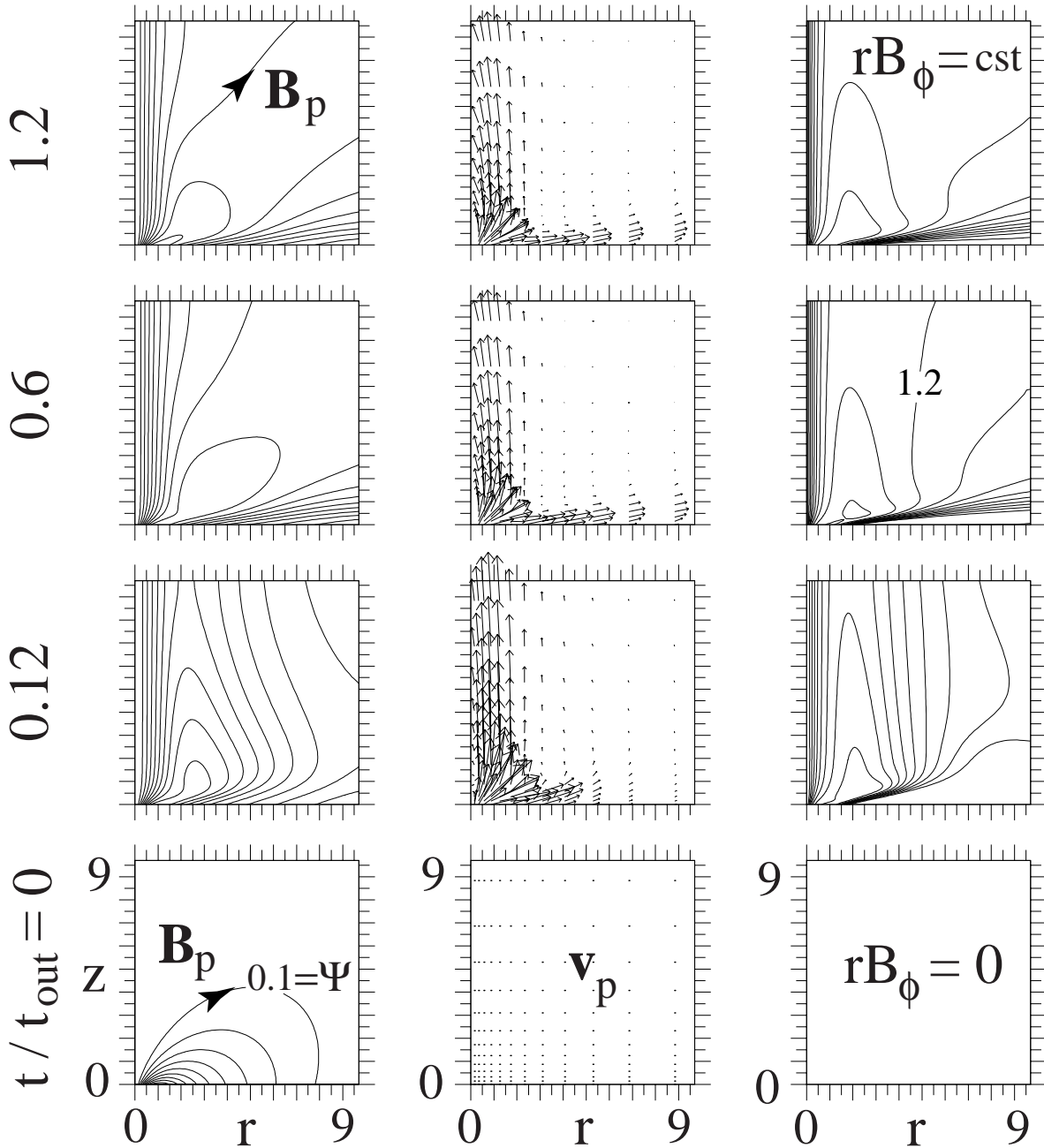


FIG. 10.—Time evolution of dipole-like field threading the disk from the initial configuration  $t = 0$  (bottom panels) to the final quasi-stationary configuration for the case of *open* outer boundaries at  $r = R_m$  and  $z = Z_m$ . Here,  $t_{\text{out}}$  is the rotation period of the disk at the outer radius  $R_m$  of the simulation region; for the parameters used,  $t_{\text{out}} \sim 200t_i$ . The initial field is shown by the dashed lines in Fig. 1. The left-hand panels show the poloidal field lines, which are the same as  $\Psi(r, z) = \text{const}$  lines;  $\Psi$  is normalized by  $\Psi_0$  [the maximum value of  $\Psi(r, z)$ ], and the spacing between lines is 0.1. The middle panels show the poloidal velocity vectors  $\mathbf{v}_p$ . The right-hand panels show the constant lines of  $-rB_\phi(r, z) > 0$  in units of  $\Psi_0/r_0$ , and the spacing between lines is 0.1. For this calculation, a  $100 \times 100$  inhomogeneous grid was used, with  $\Delta r_j$  and  $\Delta z_k$  growing with distance  $r$  and  $z$  geometrically as  $\Delta r_j = \Delta r_1 q^j$  and  $\Delta z_k = \Delta z_1 q^k$ , with  $q = 1.03$  and  $\Delta r_1 = \Delta z_1 = 0.05r_0$  (Ustyugova et al. 2000).

nated with flow speeds  $v^2 \ll v_A^2$ , where  $v_A$  is the Alfvén velocity. The field configuration is similar to that found for the high-twist GS solutions as shown in Figure 5.

Figure 10 shows the long time evolution of the coronal plasma for the case in which the outer boundaries are free (i.e., open) boundaries. These simulations evolve to a quasi-stationary final state in which most of the region is strongly field dominated. In the jet region along the  $z$ -axis, the poloidal field is collimated by the  $B_\phi$  field. We find that the profiles of  $B_\phi(r)$  and  $B_z(r)$  from the simulations (Ustyugova et

al. 2000) agree to a good approximation with equation (6) of our analytic model. The main respect in which the simulations differ from the GS solutions is that the region close to the disk where the magnetic field returns to the disk is *not* field dominated. Instead, this region has a hydromagnetic outflow from the disk. This is predicted theoretically (Blandford & Payne 1982) and observed in simulations (Ustyugova et al. 1999) to be the case when the angle  $\theta$  between the disk normal and the poloidal field lines is larger than  $30^\circ$ .

## 14. CONCLUSIONS

An ordered magnetic field threading an accretion disk can give powerful outflows or jets of matter, energy, and angular momentum. Most of the studies have been in the hydromagnetic regime, where there is appreciable mass outflow, and find asymptotic flow speeds of the order of the maximum Keplerian velocity of the disk,  $v_{Ki}$ . These flows are clearly relevant to the jets from protostellar systems that have flow speeds of the order of  $v_{Ki}$ . In contrast, observed very long baseline interferometry (VLBI) jets in quasars and active galaxies point to bulk Lorentz factors  $\Gamma \sim 10$ —much larger than the disk Lorentz factor. In the jets of gamma-ray burst sources,  $\Gamma \sim 100$ . The large Lorentz factors as well as the small Faraday rotation measures suggest that these jets are in the Poynting flux regime. This work presents self-consistent solutions for the axisymmetric, nonrelativistic plasma equilibria described by the force-free Grad-Shafranov equation. We find solutions with magnetically collimated Poynting jets where there is a *continuous* outflow of energy, angular momentum, and toroidal magnetic flux from the disk into the external space. This behavior contra-

dicts the commonly accepted “theorem” of solar plasma physics that the motion of the footpoints of a magnetic loop structure leads to a stationary magnetic field configuration with zero power, angular momentum, and flux outflows (Aly 1984, 1991).

Important issues remain to be investigated—the relativistic expansion of the head of a Poynting jet into an external medium and the three-dimensional kink instability of the jet. Further, the magnetic extraction of energy from a rotating black hole may be important (Blandford & Znajek 1977; Livio, Ogilvie, & Pringle 1999).

R. L. and M. R. thank H. Li, S. A. Colgate, and J. M. Finn for valuable discussions and hospitality at the Los Alamos National Laboratory, where this work was begun. R. L. thanks J. Chen for valuable discussions about coronal magnetic fields. This research was supported in part by NASA grants NAG5-9047 and NAG5-9735 and NSF grant AST 99-86936. M. M. R. received partial support from NSF POWRE grant AST 99-73366.

## REFERENCES

- Aly, J. J. 1984, *ApJ*, 283, 349  
 ———. 1991, *ApJ*, 375, L61  
 Bateman, G. 1980, *MHD Instabilities* (Cambridge: MIT Press)  
 Blandford, R. D., & Payne, D. G. 1982, *MNRAS*, 199, 883  
 Blandford, R. D., & Znajek, R. L. 1977, *MNRAS*, 179, 433  
 Bridle, A. H., & Eilek, J. A. 1984, in *Physics of Energy Transport in Extragalactic Radio Sources* (Greenbank: NRAO)  
 Bührke, T., Mundt, R., & Ray, T. P. 1988, *A&A*, 200, 99  
 Colgate, S. A., & Li, H. 1998, in *IAU Colloq. 195, Highly Energetic Physical Processes and Mechanisms for Emission from Astrophysical Plasmas*, ed. P. C. H. Martins, S. Tsuruta, & M. A. Weber (San Francisco: ASP), 255  
 Eikenberry, S., Matthews, K., Morgan, E. H., Remillard, R. A., & Nelson, R. W. 1998, *ApJ*, 494, L61  
 Finn, J. M., & Chen, J. 1990, *ApJ*, 349, 345  
 Gold, T., & Hoyle, F. 1960, *MNRAS*, 120, 89  
 Heyvaerts, J. 2001, *Proc. of JENAM 2000 meeting*, Moscow  
 Kadomtsev, B. B. 1963, *Rev. Plasma Phys.*, 2, 188  
 Katz, J. I. 1997, *ApJ*, 490, 633  
 Levinson, A. 1998, *ApJ*, 507, 145  
 Li, H., Lovelace, R. V. E., Finn, J. M., & Colgate, S. A. 2001, *ApJ*, 561, 915  
 Livio, M., Ogilvie, G. I., & Pringle, J. E. 1999, *ApJ*, 512, 100  
 Lovelace, R. V. E., Berk, H. L., & Contopoulos, J. 1991, *ApJ*, 379, 696  
 Lovelace, R. V. E., Newman, W. I., & Romanova, M. M. 1997, *ApJ*, 484, 628  
 Lovelace, R. V. E., Wang, J. C. L., & Sulkanen, M. E. 1987, *ApJ*, 315, 504  
 Lynden-Bell, D. 1996, *MNRAS*, 279, 389  
 Lynden-Bell, D., & Boily, C. 1994, *MNRAS*, 267, 146  
 Meier, D. L., Koide, S., & Uchida, Y. 2001, *Science*, 291, 84  
 Mirabel, I. F., & Rodríguez, L. F. 1994, *Nature*, 371, 46  
 Mundt, R. 1985, in *Protostars and Planets II*, ed. D. C. Black & M. S. Mathews (Tucson: Univ. Arizona Press), 414  
 Romanova, M. M. 1999, in *IAU Symp. 194, Active Galactic Nuclei and Related Phenomena*, ed. Y. Terzian, D. Weedman, & E. Khachikian (San Francisco: ASP), 256  
 Romanova, M. M., & Lovelace, R. V. E. 1997, *ApJ*, 475, 97  
 Romanova, M. M., Ustyugova, G. V., Koldoba, A. V., Chechetkin, V. M., & Lovelace, R. V. E. 1998, *ApJ*, 500, 703  
 Shakura, N. I., & Sunyaev, R. A. 1973, *A&A*, 24, 337  
 Sturrock, P. A. 1991, *ApJ*, 380, 655  
 Ustyugova, G. V., Koldoba, A. V., Romanova, M. M., Chechetkin, V. M., & Lovelace, R. V. E. 1999, *ApJ*, 516, 221  
 ———. 1995, *ApJ*, 439, L39  
 Ustyugova, G. V., Lovelace, R. V. E., Romanova, M. M., Li, H., & Colgate, S. A. 2000, *ApJ*, 541, L21